A Wearable Platform for Real-Time Control of a Prosthetic Hand by High-Density EMG

Ricardo G. Molinari, Valeria Avilés-Carrilo, Guilherme A. G. De Villa, and Leonardo A. Elias, *Member, IEEE*

***Abstract*— This study presents a wearable platform for high-density surface electromyography (HD sEMG) and real-time myoelectric control of a hand prosthesis. The system features two 64-channel RHD2164 analog front-ends (totaling 128 channels) integrated with a Zynq UltraScale+ MPSoC for heterogeneous computing. The PYNQ-based framework offers a Python/Linux environment for designing scalable and flexible multi-purpose algorithms. Experiments with 21 healthy subjects performing eight motor tasks (finger flexion/extension, thumb opposition, and prehension patterns) at two frequencies (0.50 Hz and 0.75 Hz) demonstrated the system's capabilities in both HD sEMG recording and real-time prosthetic control for a single degree of freedom (1-DoF). Signal quality metrics exceeded recommended thresholds (Signal-to-noise Ratio: 13.93 ± 7.51 dB; Signal-to-motion-artifact Ratio: 25.18 ± 5.18 dB), validating the dual-front-end architecture. The processing pipeline combining reinforced electrode signal adaptation (RESA), non-negative matrix factorization (NMF), and Kalman filtering achieved high similarity between estimated and reference signals for the test data, assessed using the maximum normalized cross-correlation (XC_{max}), with values from 0.54 ± 0.22 to 0.80 ± 0.16. The coefficient of determination (R^2) for HD sEMG signal reconstruction ranged from 0.87 ± 0.09 to 0.95 ± 0.03, with higher values observed in tasks involving prehension patterns. The platform demonstrated scalable real-time performance, with total latency from acquisition to command output ranging from 63.3 ± 1.0 ms (30 ms buffer) to 219.1 ± 4.5 ms (150 ms buffer), while maintaining temporal alignment (lag at XC_{max}: 0.02 ± 2.09 s). The platform's heterogeneous architecture enabled local execution of all processing stages (at 2052.52 Hz sampling rate/channel), with the FPGA handling signal acquisition and Arm Cortex-A53 cores performing motor intention decoding, supporting future integration of adaptive multi-DOF control for advanced prosthetic applications.**

***Index Terms*— Heterogeneous Computing; Myoelectric Control; Prosthesis; Surface EMG; Wearable Technology.**

This work was supported by the Brazilian Public Ministry of Work (contract number 002118.2019). Leonardo A. Elias is a Research Productivity Fellow of CNPq (Brazilian NSF, process number 316320/2023-4). *(Corresponding author: L.A. Elias)*

Ricardo G. Molinari, Valeria Avilés-Carrillo, and Leonardo A. Elias are with the Department of Electronics and Biomedical Engineering, School of Electrical and Computer Engineering, University of Campinas, Campinas, SP 13083-852 Brazil, and with the Neural Engineering Research Laboratory, Center for Biomedical Engineering, University of Campinas, Campinas, SP 13083-881 Brazil (molinari@unicamp.br, v222717@dac.unicamp.br, and leoelias@unicamp.br). Guilherme Augusto Gomes De Villa was with the Neural Engineering Research Laboratory, Center for Biomedical Engineering, University of Campinas, Campinas, SP 13083-881, Brazil. He is now with the State University of Goiás, Itaberaí, GO 76630-000, Brazil (e-mail: guilhermea1991@gmail.com).

I. INTRODUCTION

HIGH-DENSITY surface electromyography (HD sEMG) has become a key technology for non-invasive neuromuscular signal acquisition, enabling advanced control of upper-limb prostheses [1]. By capturing spatially detailed muscle activation patterns with dense electrode grids, HD sEMG enables the accurate decoding of user intent, which is essential for intuitive and precise prosthetic control. This is particularly relevant for transradial amputees, for whom restoring fine finger movements and grip force modulation remains challenging [2]. Nevertheless, rejection rates of below-elbow prostheses remain as high as 71.4%, mainly due to issues of comfort, weight, and limited functionality [3].

Despite promising laboratory results, myoelectric prostheses still face deficits in dexterity and responsiveness, which hinder their real-world adoption [4]. Achieving biomimetic control demands both high-quality HD sEMG acquisition and real-time algorithms capable of interpreting high-dimensional data. Machine-learning approaches, including neural networks [5], have shown promise; however, their computational cost poses a challenge to their integration into wearable devices.

Real-time control on embedded platforms demands not only low latency and energy efficiency but also resilience to unreliable wireless links. Transmitting raw HD sEMG to external computers or the cloud increases data payload and power consumption, while leaving performance vulnerable to wireless dropouts and fluctuating bandwidth—conditions that can disrupt critical control loops and compromise safety [6]. Edge-based processing mitigates these challenges by minimizing latency, maintaining stable operation despite wireless instability, and supporting reliable closed-loop control [7].

This work presents a 128-channel HD sEMG acquisition and processing device with heterogeneous local computing. The platform integrates high-density signal acquisition with onboard real-time processing to implement advanced myoelectric control strategies directly on the device. We validated the system using a proportional movement-intention decoding (PMID) approach for a single degree of freedom (1-DoF), demonstrating its potential to support intuitive control of a prosthetic hand, thereby bridging the gap between research and real-world application for transradial amputees.

II. ACQUISITION AND PROCESSING SYSTEM

Fig. 1 shows the schematic diagram of the HD sEMG signal acquisition and processing platform developed for real-time control of prosthetic hands. The platform consists of

two analog front-ends and a heterogeneous computing system. The analog front-ends used RHD2164 devices (Intan Technologies, USA), each connected to a 64-channel electrode grid (GR10MM0808, OT Bio elettronica, Italy). Each front-end amplifies, filters, digitizes, and transmits the myoelectric signals to the processing system.

The processing system uses the FZ3 CARD development board (MYiR Tech Ltd., China), which incorporates the Zynq UltraScale+ Multiprocessor System-on-Chip (MPSoC) (Advanced Micro Devices Inc., USA). The Zynq UltraScale+ integrates an application processing unit (APU) and a field-programmable gate array (FPGA) in a single device. The FPGA acts as a protocol bridge between the analog front-ends and the APU. Also, the FPGA enables direct memory access (DMA) to the data registers. The APU consists of four Arm Cortex-A53 cores and runs a Linux Ubuntu operating system based on a customized version of the PYNQ (Python Productivity for Zynq) framework. This setup orchestrates the entire platform, including hosting a graphical user interface (GUI), configuring the analog front-ends, initializing the FPGA, monitoring battery status, and executing the PMID loop.

The estimated proportional movement intention (see description below) was transmitted via the SN65HVD1050 transceiver (Texas Instruments, USA), using the Controller Area Network (CAN) protocol, to a modified version of the open-source Brunel Hand 2.0 (Open Bionics, UK). The system's GUI, developed in Jupyter Notebook, was accessed remotely through the VAP11G-300 Wi-Fi bridge (Vonets Network Co. Ltd., China) using a browser connected to the same network. The GUI enabled the initial configuration of the devices, operational control of the platform, and visualization of the HD sEMG signals. Rechargeable lithium-ion batteries (model 369108, Hamilton Medical, Switzerland), consisting of three cells in series and two sets in parallel (3S2P, with a nominal voltage of 10.8 V and 72 Wh), along with a battery management system (BMS) BQ20Z95 (Texas Instruments, USA), were used to power the platform. The FZ3 CARD board includes the power management integrated circuit (PMIC) TPS650864 (Texas Instruments, USA), which manages power delivery to the MPSoC and other onboard devices. In parallel, the battery also supplies power to the bionic hand via a Buck-Boost DC/DC converter module (XL6009, KylinChip Electronic, China), which regulates the voltage to 10.8 V (as shown in Fig. 1 by the red arrows).

A. The Analog Front-End Module

Table I presents critical parameters for HD sEMG acquisition and compares the recommended features [8], [9] with the technical specifications of the RHD2164 device (as provided in its datasheet). The comparison includes aspects of analog front-end quality (such as amplitude, impedance, noise rejection, voltage range, intrinsic noise, and filtering) and analog-to-digital converter (ADC) performance, including sampling rate, resolution, and number of bits. The device employed in the platform features configurable third-order Butterworth analog band-pass filters, whose cutoff frequencies were set to 10 Hz and 500 Hz. Moreover, a first-order digital high-pass filter was activated and configured with a cutoff frequency of 10 Hz to remove oscillations and drift in the signal's baseline level. The RHD2164 operates in slave mode, with a per-channel sampling rate of 2052.52 Hz, directly determined by the frequency of commands received via the Serial Peripheral Interface (SPI) generated by the FPGA. Each RHD2164 integrates two 32-channel modules that operate in parallel, with the ADC data combined using a Double Data Rate (DDR) multiplexer for transmission via the Master Input Slave Output (MISO) channel. Low-Voltage Differential Signaling (LVDS) was employed for data transmission through 0.9-meter flexible cables (RHD SPI Interface, Intan Technologies, USA) connecting the analog front-ends to the processing system.

B. Dual-Mode FPGA Interface for RHD2164 Devices

The Advanced Extensible Interface (AXI) - DDR SPI module, implemented in the MPSoC's FPGA, was responsible for converting between the LVDS DDR SPI and AXI protocols. A finite state machine was employed to manage the bridge between these protocols, handling data alignment of the master DDR SPI interface channels, performing (de)serialization, identifying valid MISO message cycles, and configuring the operating modes: configuration and streaming. In configuration mode, the interface enables the GUI to access the registers of the RHD2164 devices for setup and calibration. In streaming mode, the module continuously generates analog-to-digital conversion commands for the RHD2164 devices and sends the results to external memory via the AXI DMA block. The AXI DMA operates cyclically based on the buffer size defined through the APU GUI. The FPGA design communicates reliably with the RHD2164 chip, with a maximum setup time of 10.40 ns and a hold time of 12 ns, which are within the operational limits specified in the chip's datasheet.

C. The Porportional Movement Intention Decoding Loop

The proportional movement intention decoding (PMID) loop utilizes successive and overlapping analysis windows of HD sEMG recordings with a duration of T_a to maximize the processing capacity of the APU [10]. The first stage of the loop implements a fourth-order Butterworth band-pass digital filter (10-500 Hz) and a 60 Hz notch filter to remove possible motion artifacts, high-frequency noise, and power line interference that may bypass the analog front-end filtering. The second stage applies the Reinforced Electrode Signal Adaptation (RESA) algorithm to remove non-stationary artifacts caused by impedance variations at the skin-electrode interface [11]. The RESA algorithm computes an adaptation weight matrix for the channels based on the similarity between a virtual reference signal (VRS) and the electrode signals. To enable real-time implementation on the proposed platform, two modifications were applied to the original algorithm [11] to reduce the processing time of computationally intensive functions. The first modification replaces the Beta distribution model used in the VRS calculation with a Gaussian distribution model. The second modification substitutes the mutual information metric with Pearson's correlation coefficient.

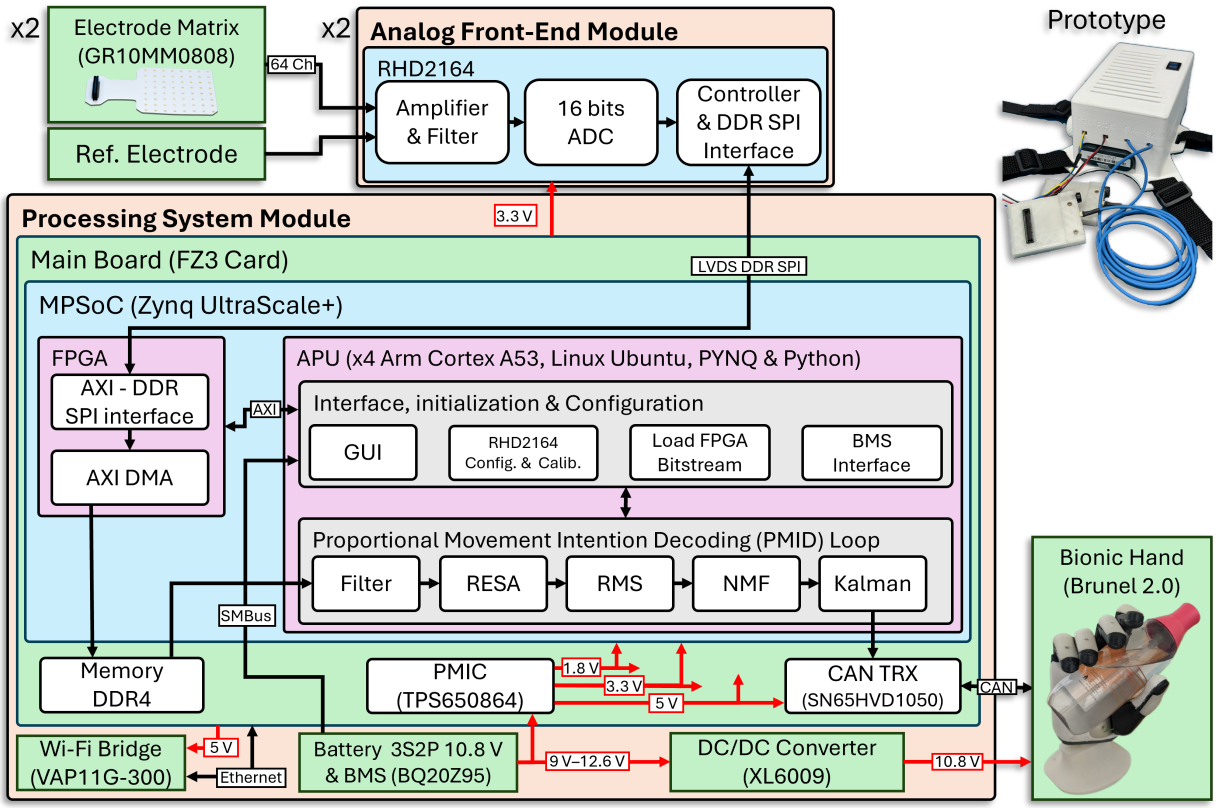

Fig. 1. Schematic diagram of the developed HD sEMG acquisition and processing platform for real-time prosthetic hand control. Two 64-channel analog front-ends amplify, filter, digitize, and transmit the signals to a heterogeneous processing system (Zynq UltraScale+ MPSoC), which combines FPGA and CPU cores running a customized Linux-based PYNQ framework. The system handles signal acquisition, movement intention decoding, GUI operation, and battery monitoring. A rechargeable Li-ion battery pack with a BMS powers the platform and the prosthetic hand, with voltage regulated for each device. The image illustrates the hardware and software components as well as the information and power flow. Wireless access to the GUI is provided via a Wi-Fi bridge. The top right corner shows the platform prototype, and the bottom right corner shows the Brunel Hand 2.0 (Open Bionics, UK) controlled by the platform.

TABLE I
COMPARISON BETWEEN RECOMMENDED HD sEMG SIGNAL ACQUISITION FEATURES AND RHD2164 SPECIFICATIONS.

Specification	**Recommendations [8], [9]**	**RHD2164**
Amplifier AC Input Voltage Range, mV	± 7.5	± 5.0
Input Impedance, MΩ	$\geq$ 80 at 50–60 Hz	1300 at 10 Hz and 13 at 1 kHz
Common-Mode Rejection Ratio (CMRR), dB	$\geq$ 90 at 50–60 Hz	82 at 50–60 Hz
Power Supply Rejection Ratio (PSRR), dB	$\geq$ 60	75
Input-Referred Noise, μV_{RMS}	$\leq$ 2.0	2.4
High-Pass Cutoff Frequency (analog prefilter), Hz	0.10–20	0.02–1000
Low-Pass Cutoff Frequency (analog prefilter), Hz	500–1000	10–20000
ADC Sampling Rate per Channel, Hz	$\geq$ 2048	up to 30000
ADC Resolution, bits	$\geq$ 12	16
Input-Referred Resolution, μV	$\leq$ 0.500	0.195

The third stage of the loop calculates the root mean square (RMS) value of the HD sEMG channels using sliding windows of duration T_a. The fourth stage decomposes the matrix into two components through non-negative matrix factorization (NMF) [12]. One component captures finger flexion, thumb opposition, or grasp-closing movements, while the other represents finger extension, thumb reposition, or grasp-opening movements. The algorithm assigned each component to a movement direction by analyzing the phase of the cross-spectral density between its temporal signal and the task's command signal (described in Section III-B). This directional mapping subsequently derived the proportional movement intention from the difference between the two components and standardized the resulting signal to have zero mean and unit variance. The fifth and final stage applies a one-dimensional Kalman filter [13] (without a dynamic model) to reduce

noise associated with the movement intention prediction. The process noise variance was set to 10^{-4}, and the measurement noise variance as 10^{-2}.

III. EXPERIMENTAL EVALUATION

A. Participants

Twenty-one healthy participants (10 women, 11 men) participated in the experimental protocol. Participants' demographics are (mean $\pm$ standard deviation): 27.19 ± 6.55 years, body weight of 73.52 ± 16.06 kg, and height of 1.68 ± 0.11 m. Only one participant reported being left-handed. None of the participants had a history of neuromuscular or joint disorders that affected their dominant hand. The study was approved by the Research Ethics Committee of the University of Campinas (CAAE 80299124.2.1001.5404) on 24 October 2024, and all participants provided informed consent before the experiments.

B. Experimental Protocol

The electrode grids were placed centrally over the Extensor Digitorum Communis (EDC) and Flexor Digitorum Superficialis (FDS) muscles [14] after skin abrasion with an exfoliating paste and cleansing with 70% alcohol. Reference electrodes were attached to the wrist using a water-moistened conductive strap. Participants followed instructions to replicate dynamic, sinusoidal finger movements displayed by a virtual model of the bionic hand on a monitor placed in front of them (Fig. 2) while seated comfortably in a chair with their elbow resting on a height-adjustable table. Tasks began with the fingers fully extended, followed by the execution of eight movement patterns: flexion and extension of the index finger, the middle finger, and the ring and little fingers simultaneously; thumb opposition and retraction; pinch grasp and release with the index finger and thumb, and with the middle finger and thumb; tripod pinch with the index, middle, and thumb fingers; and 5-finger grasp. Sinusoidal finger movements were displayed at 0.50 Hz and 0.75 Hz, yielding 16 trials per set. Each participant completed three sets, totaling 48 tasks. Each task lasted 45 seconds, with at least 30 seconds of rest between tasks. The order of the tasks was randomized, and HD sEMG signals were also recorded at rest to assess signal quality.

The designed platform synchronized the start of HD sEMG signal recording, the virtual bionic hand movements shown on the monitor, and the motion capture system (Fig. 3). Synchronization signals were transmitted over Wi-Fi using the TCP/IP protocol to the monitor interface, developed with Unity Engine (Unity Technologies, USA), and via the UDP/IP protocol to the Vicon Vero 2.2 motion capture system (Vicon Motion Systems, UK). The kinematic data were processed using a custom-made trigonometric model that estimates 1-D metacarpophalangeal joint angles.

C. HD sEMG Properties

The analysis examined the HD sEMG recordings obtained with the new platform in both time and frequency domains.

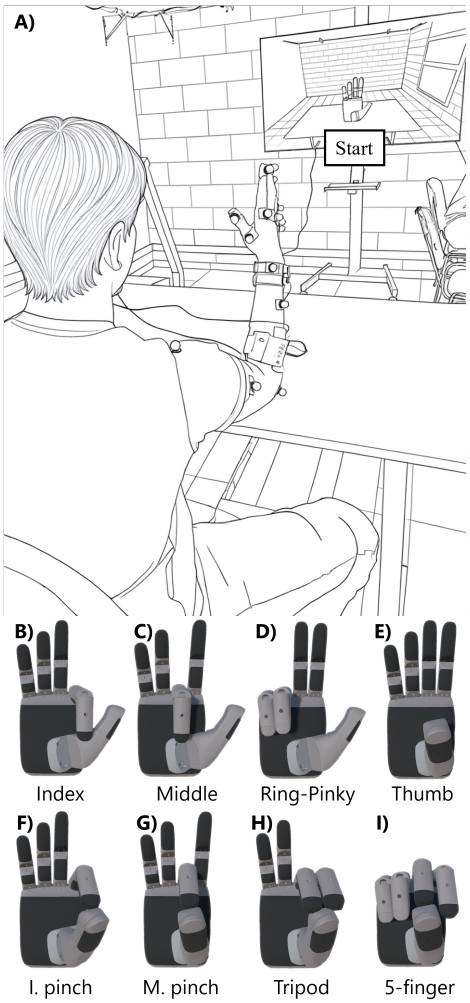

Fig. 2. (A) Experimental setup. Each participant was instructed to follow sinusoidal dynamic movements displayed on a screen. HD sEMG of EDC and FDS muscles were recorded synchronously with the virtual bionic hand movements, along with hand markers to estimate joint angles by a Vicon motion capture system. Panels B to I illustrate the eight movements studied: (B) Index finger flexion; (C) Middle finger flexion; (D) Ring and little finger flexion; (E) Thumb opposition; F) Pinch grasp with the index finger; (G) Pinch grasp with the middle finger; (H) Tripod grasp; (I) 5-finger grasp.

The signals underwent only the analog and digital filtering stages integrated into the system's front-end, with no additional filtering applied during the processing of properties and quality metrics. The evaluation of HD sEMG characteristics included the peak-to-peak amplitude of the sEMG ($sEMG_{P2P}$), the mean value of the $sEMG_{RMS}$, the coefficient of variation (CoV) of the $sEMG_{RMS}$, and the median frequency (MF) of the sEMG power spectral density ($sEMG_{PSD}$). Calculation of the $sEMG_{RMS}$ employed 300 ms windows. The PSD was estimated using Welch's method with 2-second Hanning windows without overlap.

D. HD sEMG Quality Assessment

The assessment of HD sEMG data quality utilized metrics derived from the $sEMG_{PSD}$, which quantified the contamination level of each recording, including motion

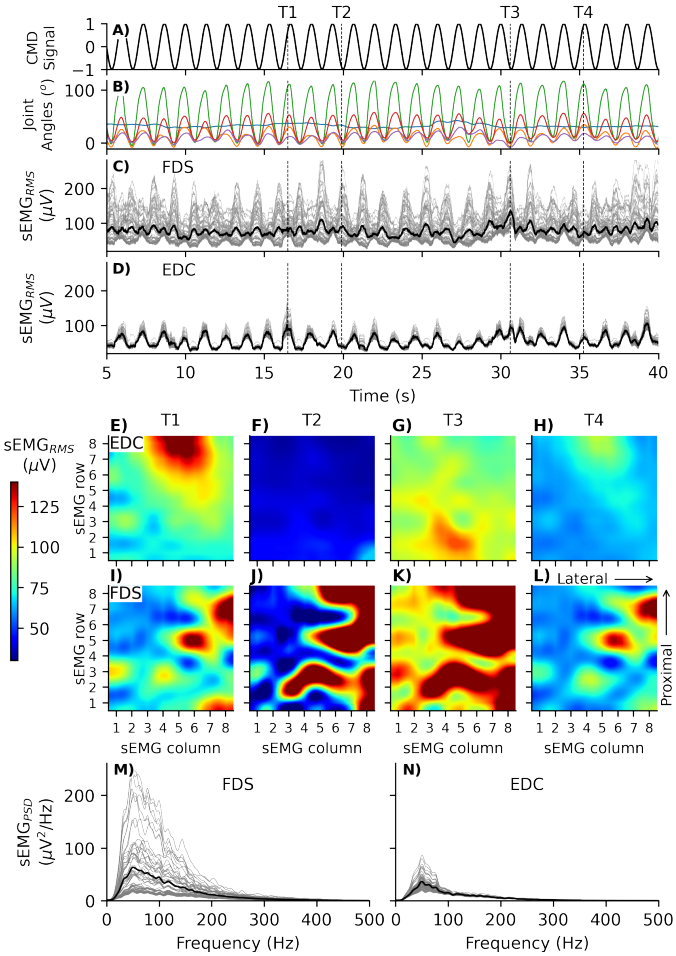

Fig. 3. Example of the recordings obtained during the flexion-extension task of the middle finger at 0.75 Hz. (A) Command signal controlling the position of the fingers of the virtual bionic hand displayed on the screen. (B) Metacarpophalangeal joint angles of the middle (green), ring (red), index (orange), thumb (blue), and little (purple) fingers. (C) $\boldsymbol{sEMG_{RMS}}$ from the electrode grid positioned over the FDS muscle (gray), along with the average $\boldsymbol{sEMG_{RMS}}$ across all channels (black). (D) $\boldsymbol{sEMG_{RMS}}$ from the electrode grid positioned over the EDC muscle (gray), and the corresponding average signal (black). (E) to (G) $\boldsymbol{sEMG_{RMS}}$ activation maps from the electrode grid over the EDC muscle. (I)-(L) $\boldsymbol{sEMG_{RMS}}$ activation maps from the electrode grid over the FDS muscle. (M) and (N) $\boldsymbol{sEMG_{PSD}}$ (Power Spectral Density) of the electrode grid over the FDS and EDC muscles, respectively (gray), along with their mean PSD (black).

artifacts, power line interference, noise, and intrinsic distortions of the acquisition system [15]. Six quality metrics were calculated (Tab. II): Signal-to-Noise Ratio (SNR); Signal-to-Motion-artifact Ratio (SMR); Signal-to-Power-line-interference Ratio (SPR); Signal-to-High-frequency-noise Ratio (SHR); Spectrum Maximum-to-Minimum Drop in Power Density (SMMD); and Power Spectrum Deformation Ratio (PSDR). Evaluation of the results considered acceptable levels previously defined in the literature, when available [16], [17]. The distribution of SNR values was analyzed based on the taxonomy proposed by [17], where values below 1.8 dB do not necessarily indicate unacceptable signals but a low signal-to-noise ratio, suggesting a lack of relevant myoelectric activity for control applications; signals with SNR between 1.8 dB and 10 dB are acceptable; signals with SNR between 10 and 18 dB demonstrate minimized noise interference, rendering them highly suitable for precise control; and values above 18 dB indicate negligible noise, characterizing high-quality signals ideal for myoelectric control systems.

TABLE II
SPECTRAL METRICS USED TO EVALUATE THE QUALITY OF MYOELECTRIC SIGNALS.

Metric (Abbreviation)	Equation	Acceptable Level [16], [17]
Signal-to-Noise Ratio (SNR)	$\frac{P_{signal}}{P_{rest}}$	> 1.8 dB
Signal-to-Motion-artifact Ratio (SMR)	$\frac{P_{signal}}{P_{0-20\,\mathrm{Hz}}}$	> 12 dB
Signal-to-Power-line-interference Ratio (SPR)	$\frac{P_{signal}}{P_{60,120,\ldots}}$	N/A
Signal-to-High-frequency-noise Ratio (SHR)	$\frac{P_{signal}}{P_{500-1026\,\mathrm{Hz}}}$	> 15 dB
Spectrum Maximum-to-Minimum Drop in Power Density (SMMD)	$\frac{MPD_{highest}}{MPD_{lowest}}$	> 30 dB
Power Spectrum Deformation Ratio (PSDR)	$\frac{(M_2/M_0)^{0.5}}{M_1/M_0}$	< 1.4

P_{signal} and P_{rest} are the total signal power measured during the task and at rest, respectively. P_{0-20Hz} represents the power below 20 Hz. $P_{60,120\ldots Hz}$ corresponds to the power at 60 Hz and its harmonics up to half the sampling frequency. $P_{500-1026}$ denotes the sum of the power in frequencies greater than 500 Hz. MPD represents the mean power density of 13 consecutive points shifted across all frequencies. M_n is the n-th order spectral moment.

E. Proportional Movement Intention Decoding Loop

The estimation time (T_e) of the PMID loop and the contribution of each stage (filters, RESA, RMS, NMF, Kalman, and CAN) were evaluated for analysis window lengths (T_a) of 30, 60, 90, 120, and 150 ms. We calculated the accumulated time from the start of the acquisition window to the end of processing ($T_a + T_e$) and the ratio T_e/T_a. This ratio indicates the degree of overlap between consecutive windows, as the step between them approximates T_e. Values above 1 imply no overlap—risking loss of transient signal information—while values below 1 indicate overlapping windows, which enhance temporal resolution.

CAN transmission time was measured 10 times using a RIGOL MSO5074 oscilloscope and an ESP32 WROOM-32E microcontroller. It was defined as the interval between the rising edge of a step signal generated by the MPSoC just before sending a CAN message and the rising edge of a signal generated by the microcontroller upon message reception.

For NMF training, the first 5 s of HD sEMG recordings were discarded to avoid transients, and the following 20 s were used for model training. The analysis window T_a defined the sliding window for RMS calculation to ensure consistent temporal parameters during testing. The coefficient of determination (R^2) quantified how well the NMF-reconstructed $sEMG_{RMS}$ signals matched the original data.

During training, the RESA weight matrix was updated every 30 ms, and the final weights served as the initial values for

testing. The last 20 s of each trial (testing interval) assessed the PMID loop's ability to track oscillations in the command signal. In testing, the PMID loop processed consecutive windows of length T_a using the spatial component matrix learned during training (Fig. 4A–D).

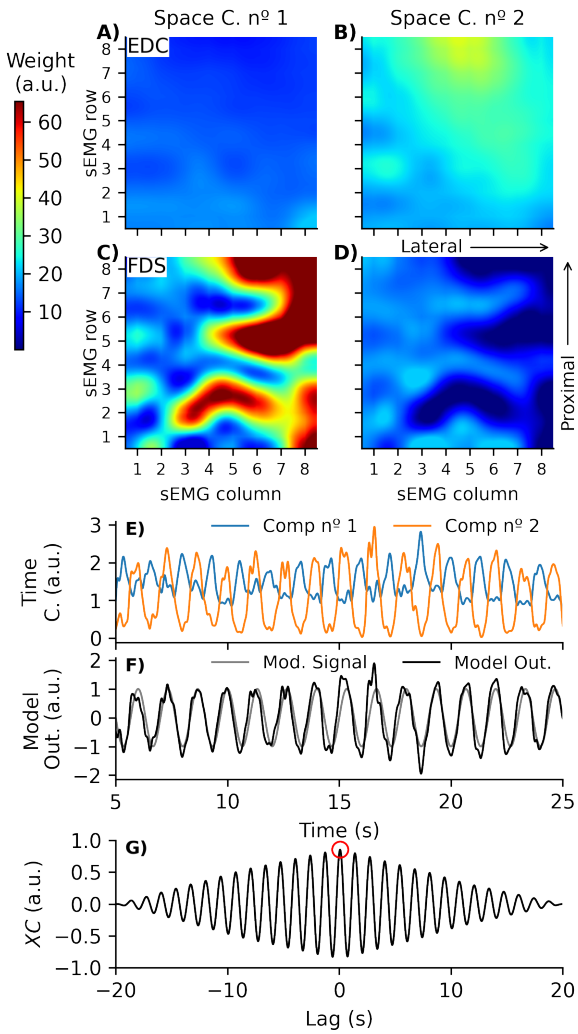

Fig. 4. Example of the NMF decomposition and similarity evaluation between model output and command signals. (A and C) First spatial components extracted from the electrode grids over the EDC and FDS. (B and D) The second spatial components from the EDC and FDS muscles. (E) First and second temporal components. (F) Command signal of the virtual bionic hand (gray) and PMID loop output (black). (G) Normalized cross-correlation function between command and estimated signals (black) with $\boldsymbol{XC_{max}}$ highlighted (red circle).

F. Statistical Analysis

Before statistical analysis, the normality of data from HD sEMG properties and the similarity between the estimated proportional movement intention and the command signals were assessed using the D'Agostino-Pearson test. In both cases, the data consistently failed the normality assumption across all metrics ($p < 0.001$), indicating the need to adopt non-parametric hypothesis tests.

The influence of task type and task frequency on HD sEMG properties was analyzed using a multifactorial Kruskal–Wallis test. Given the huge sample size, all comparisons were statistically significant ($p < 0.001$) across all metrics. Therefore, the analysis focused on reporting the effect size using Epsilon squared (ε^2), which provides a robust measure independent of the sample size [18]. The effect size was considered negligible when $\varepsilon^2 < 1\%$, small for $1\% \leq \varepsilon^2 < 8\%$, medium for $8\% \leq \varepsilon^2 < 26\%$, and large for $\varepsilon^2 \geq 26\%$ [19].

Similarity between estimated proportional movement intention and command signals was quantified by the maximum normalized cross-correlation (XC_{max}) on the test data (Fig. 4G). The effect of T_a on XC_{max} was analyzed via the Kruskal–Wallis test. The effects of task type and frequency on XC_{max}, training R^2, and the lag at XC_{max} during testing were assessed with a multifactorial Kruskal–Wallis test at $T_a = 60$ ms, followed by Dunn's post hoc test for pairwise comparisons.

All descriptive statistics are reported as mean $\pm$ standard deviation. Statistical significance was considered when $p < 0.05$.

IV. RESULTS

A. HD sEMG Properties

Out of the 129,024 signals recorded during platform evaluation, only two channels (0.002 %) exceeded the amplifier's linear range (±5 mV). At rest, HD sEMG showed $sEMG_{P2P}$ of 244.15 ± 253.14 µV, $sEMG_{RMS}$ of 15.62 ± 11.02 µV, and $sEMG_{MF}$ of 128.90 ± 37.18 Hz. The low $sEMG_{RMS}$ confirmed negligible muscle activity, defining the baseline for SNR calculation.

Dynamic tasks at 0.75 Hz produced higher $sEMG_{P2P}$ amplitudes (1.36 ± 0.64 mV) than at 0.50 Hz (1.13 ± 0.55 mV; Fig. 5A), with a small effect size of frequency ($\varepsilon^2 = 4.37\%$). Mean $sEMG_{RMS}$ followed the same trend: 82.60 ± 36.69 µV at 0.75 Hz vs. 66.71 ± 29.07 µV at 0.50 Hz ($\varepsilon^2 = 6.83\%$). Task type had a medium effect size on $sEMG_{P2P}$ ($\varepsilon^2 = 10.80\%$) and a small effect size on mean $sEMG_{RMS}$ ($\varepsilon^2 = 6.75\%$). The interaction of task type and frequency had medium effect sizes ($sEMG_{P2P}$: $\varepsilon^2 = 15.37\%$; $sEMG_{RMS}$: $\varepsilon^2 = 13.68\%$). The 5-finger grasp task produced the highest mean $sEMG_{RMS}$ (0.75 Hz: 96.34 ± 47.25 µV; 0.50 Hz: 73.29 ± 30.11 µV), whereas the lowest values occurred in the index (0.75 Hz: 68.65 ± 26.53 µV) and thumb (0.50 Hz: 55.93 ± 25.04 µV) tasks (Fig. 5B).

Kruskal–Wallis analysis revealed a large effect of task type on $sEMG_{RMS}$ CoV ($\varepsilon^2 = 35.28\%$), a negligible effect of frequency ($\varepsilon^2 = 0.02\%$), and a large task type and frequency interaction ($\varepsilon^2 = 35.47\%$), indicating that CoV primarily depended on task type, with higher variability during grasping. The $sEMG_{RMS}$ CoV was consistently high for the 5-finger grasp (0.50 Hz: $51.8 \pm 18.0\%$; 0.75 Hz: $50.1 \pm 13.1\%$) and low in single-finger tasks (e.g., index at 0.75 Hz: $24.8 \pm 7.7\%$; middle at 0.50 Hz: $28.7 \pm 10.6\%$).

The $sEMG_{PSD}$ exhibited the expected monopolar pattern with power concentrated between 20–150 Hz [20], [21]. Kruskal–Wallis revealed small effect sizes of task type ($\varepsilon^2 = 7.38\%$) and frequency ($\varepsilon^2 = 1.00\%$), and a medium effect size for the interaction between task type and frequency

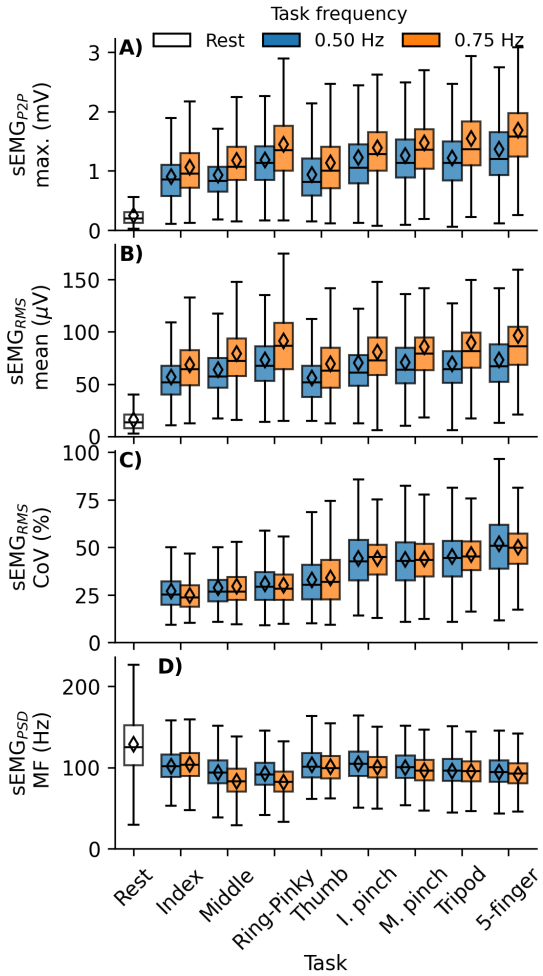

Fig. 5. Distributions of HD sEMG signal properties by task type and movement frequency ($\boldsymbol{N = 8,064}$). (A) Peak-to-peak amplitude ($\boldsymbol{sEMG_{P2P}}$), (B) mean $\boldsymbol{sEMG_{RMS}}$, (C) coefficient of variation (CoV) of $\boldsymbol{sEMG_{RMS}}$, (D) median frequency ($\boldsymbol{sEMG_{PSD}}$).

($\varepsilon^2 = 9.20\%$). Median frequency ($sEMG_{MF}$) decreased by approximately 10 Hz in middle and ring–pinky tasks at 0.75 Hz vs. 0.50 Hz (e.g., middle: 83.14 ± 22.84 Hz vs. 93.78 ± 21.58 Hz), , whereas other tasks showed smaller changes (index: 103.94 ± 20.75 Hz vs. 101.72 ± 22.98 Hz; thumb: 100.80 ± 18.66 Hz vs. 103.72 ± 21.61 Hz; Fig. 5D.

B. HD sEMG Quality Assessment

The analysis of the distribution of quality metric values for the HD sEMG signals (Fig. 6) indicated that all metrics exceeded their respective acceptance thresholds. The SNR (Fig. 6A) showed a mean value of 13.93 ± 7.51 dB, reflecting the overall quality of the acquired signals. Only $2.76 \pm 9.32\%$ of the channels exhibited an SNR below 1.8 dB, suggesting a small percentage of functionally irrelevant signals for control purposes. Approximately $30.58 \pm 34.12\%$ of the signals fell within the 1.8 to 10 dB range, indicating suitability for myoelectric control applications. The highest proportion of channels ($39.66 \pm 35.03\%$) exhibited SNR values between 10 and 18 dB, a range where noise impact on extracted sEMG parameters is considered minimal. Finally, $27.00 \pm 39.35\%$ of the channels showed an SNR above 18 dB, indicating negligible noise presence and high-quality signals suitable for myoelectric control purposes. The SNR values close to the acceptance threshold were expected, given the low-intensity contractions during the dynamic movements employed in our study, with $sEMG_{RMS}$ values below those observed in isometric tasks at 10% of maximum voluntary contraction [22].

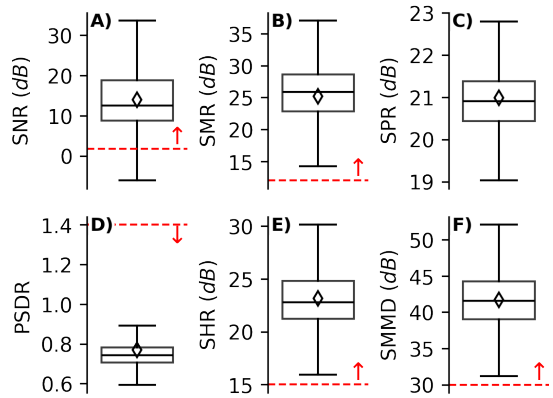

Fig. 6. Distributions of spectral quality metrics of the HD sEMG signals. Red dashed lines and arrows are shown only when acceptable thresholds are reported in the literature [17]. Arrows indicate the direction of acceptable values. (A) Signal-to-Noise Ratio (SNR). (B) Signal-to-Motion Artifact Ratio (SMR). (C) Signal-to-Power Line Interference Ratio (SPR). (D) Power Spectrum Deformation Ratio (PSDR). (E) Signal-to-High Frequency Noise Ratio (SHR). (F) Spectrum Maximum-to-Minimum Drop in Power Density (SMMD).

The SMR metric (Fig. 6B) showed a value of 25.18 ± 5.18 dB, with only $2.44 \pm 14.55\%$ of channels falling below the 12 dB threshold, suggesting that motion artifacts were minimal in the recorded data. The SPR values (Fig. 6C), which quantify power line interference at 60 Hz and its harmonics, were 20.99 ± 1.30 dB. While no established threshold exists for this metric in the literature, a visual examination of the $sEMG_{PSD}$ reveals negligible interference. The PSDR metric (Fig. 6D) had a value of 0.77 ± 0.22, with $98.67 \pm 11.03\%$ of channels below the recommended threshold of 1.4 [16], indicating a high spectral quality of the signals. The SHR metric (Fig. 6E) yielded a value of 23.16 ± 2.85 dB, with $99.81 \pm 1.08\%$ of channels exceeding the 15 dB threshold, indicating a negligible presence of high-frequency noise in the signals. The SMMD metric achieved a mean value of 41.71 ± 4.69 dB, with $99.20 \pm 1.86\%$ of channels surpassing the 30 dB threshold, indicating that nearly all signals exhibit power spectra properly sampled across the frequency range corresponding to sEMG signals.

C. Proportional Movement Intention Decoding Loop

The developed platform successfully controlled the bionic hand in real time, with the PMID loop output effectively modulating the prosthetic hand actuators (Fig. 7; see supplementary videos). Figure 8 summarizes the estimation time (T_e) and total processing time ($T_a + T_e$) of each PMID loop stage for different analysis windows (T_a). Processing times for filters, RESA, and RMS increased with T_a, while NMF, Kalman,

and CAN remained nearly constant. RESA had the highest processing time (17.69 ± 0.82 ms to 35.34 ± 4.36 ms), followed by filtering (9.21 ± 0.17 ms to 22.34 ± 0.70 ms) and RMS (1.39 ± 0.04 ms to 6.26 ms). NMF, Kalman, and CAN times were 3.34 ± 0.31 ms, 0.05 ± 0.02 ms, and 1.79 ± 0.55 ms, respectively. T_e ranged from 33.30 ± 1.01 ms to 69.11 ± 4.47 ms. Total control latency ($T_a + T_e$) increased from 63.30 ± 1.01 ms ($T_a = 30$ ms) to 219.11 ± 4.47 ms ($T_a = 150$ ms). The T_e/T_a ratio exceeded 1 only at $T_a = 30$ ms, indicating no overlap and potential loss of transient information. For $T_a \geq 60$ ms, the ratio dropped below 1 (0.76–0.46), reflecting an increasing overlap and improved temporal resolution.

Figure 9 shows R^2 and XC_{max} distributions as a function of T_a. R^2 slightly increased with larger windows (0.89 ± 0.07 to 0.94 ± 0.07). XC_{max} during training rose from 0.51 ± 0.19 to 0.67 ± 0.19, likely due to reduced RMS noise with higher T_a. XC_{max} for the test data remained unchanged ($\sim 0.66 \pm 0.20$), with no significant differences across T_a (Kruskal–Wallis, $p = 0.197$, $\varepsilon^2 = 0.12\%$), indicating that model generalization was unaffected.

Figure 10 presents the performance of the PMID loop across motor tasks and execution frequencies for $T_a = 60$ ms. The Kruskal–Wallis test revealed that task type had a large effect on R^2 ($p < 0.001$, $\varepsilon^2 = 28.94\%$), frequency had no significant effect ($p = 0.053$, $\varepsilon^2 = 0.37\%$), and the interaction between task type and frequency was significant with a large effect size ($p < 0.001$, $\varepsilon^2 = 29.53\%$), indicating that the influence of frequency depended on the specific task. Grasping tasks consistently showed the highest reconstruction quality ($R^2 = 0.95 \pm 0.03$ for the 5-finger grasp at 0.75 Hz). In contrast, non-grasping movements (index, middle, and ring–pinky fingers) exhibited lower performance ($R^2 = 0.87 \pm 0.09$ for index flexion–extension at 0.50 Hz).

Kruskal–Wallis analysis of XC_{max} for the test data revealed significant effects of task type ($p < 0.001$, $\varepsilon^2 = 11.70\%$), frequency ($p = 0.003$, $\varepsilon^2 = 0.87\%$), and the interaction between task type and frequency ($p < 0.001$, $\varepsilon^2 = 12.92\%$). The middle finger task at 0.50 Hz exhibited the highest similarity between model output and command signal (0.80 ± 0.16). In contrast, the index finger task at 0.75 Hz showed the lowest similarity (0.54 ± 0.22) compared with the other tasks.

Analysis of the cross-correlation lags showed values near zero for all tasks and frequencies (0.02 ± 2.09 s). Kruskal–Wallis tests indicated no significant effects of task type ($p = 0.578$, $\varepsilon^2 = 0.56\%$), frequency ($p = 0.459$, $\varepsilon^2 = 0.05\%$), or their interaction ($p = 0.754$, $\varepsilon^2 = 1.09\%$), confirming minimal temporal offset in model output.

V. DISCUSSION

This work demonstrates the design and validation of a wearable HD sEMG acquisition and processing platform with a heterogeneous architecture that enables real-time estimation of one degree-of-freedom (1-DoF) proportional movement intention. The system consistently produced outputs closely matching the command signals across specific hand motor tasks, while maintaining processing latencies well within real-time control requirements. Although the algorithm cannot yet represent coordinated and proportional multi-finger movements, it effectively handles 1-DoF motor tasks and establishes a robust foundation for the development of more advanced control strategies.

A. Technological Framework

The primary contribution of this work was the development and validation of a wearable platform for high-density myoelectric control of a prosthetic device, utilizing a heterogeneous computing architecture. Unlike most solutions reported in the literature, which rely on wearable devices with external processing for high-density signal acquisition [23], [24], the proposed system performs both acquisition and processing entirely embedded on the device. This design enables real-time, local algorithm execution, reducing latency and enhancing system autonomy, while providing a technical foundation for scalable and reconfigurable architectures. By integrating analog circuits for HD sEMG signal acquisition with an adaptive MPSoC, the platform supports continuous signal capture and processing under realistic usage conditions, effectively addressing challenges related to connectivity, mobility, and dependence on external computing resources [25], [26].

B. HD sEMG Properties and Quality Assessment

The acquired signals exhibited amplitudes well below the full scale of the acquisition system, indicating a robust operational margin and absence of saturation for the analyzed tasks. However, more intense muscle contractions, approaching maximum voluntary contraction, were not assessed. Despite relatively low average $sEMG_{RMS}$ values, consistent variations across tasks were observed, as reflected by the coefficient of variation ($sEMG_{RMS}$ CoV), demonstrating the system's sensitivity to varied levels of muscle activation depending on the executed motor tasks. The reduced amplitude observed during thumb opposition movements likely arises from the predominant involvement of intrinsic hand muscles, which are located distally within the hand and originate near the carpal bones. Because these muscles lie far from the electrode grids placed on the proximal forearm, the sEMG signals they generate are attenuated compared to signals from the more proximal and thicker extrinsic forearm muscles [27].

Higher mean $sEMG_{RMS}$ values at increased task frequencies reflect the increased movement cadence, which demands greater muscle recruitment to execute faster movements. This increased activation results in larger signal amplitudes, consistent with evidence showing a strong correlation between movement speed and surface EMG activity, where higher velocities systematically elicit stronger muscular responses [28].

Overall, the spectral quality metrics of the signals were quite satisfactory, showing negligible contamination by noise and artifacts, surpassing the minimum (or maximum for the PSDR) acceptability thresholds suggested in the literature [17]. Therefore, this initial investigation confirmed that the developed platform is well-suited for real-time myoelectric control applications and neurophysiological analysis of HD EMG signals.

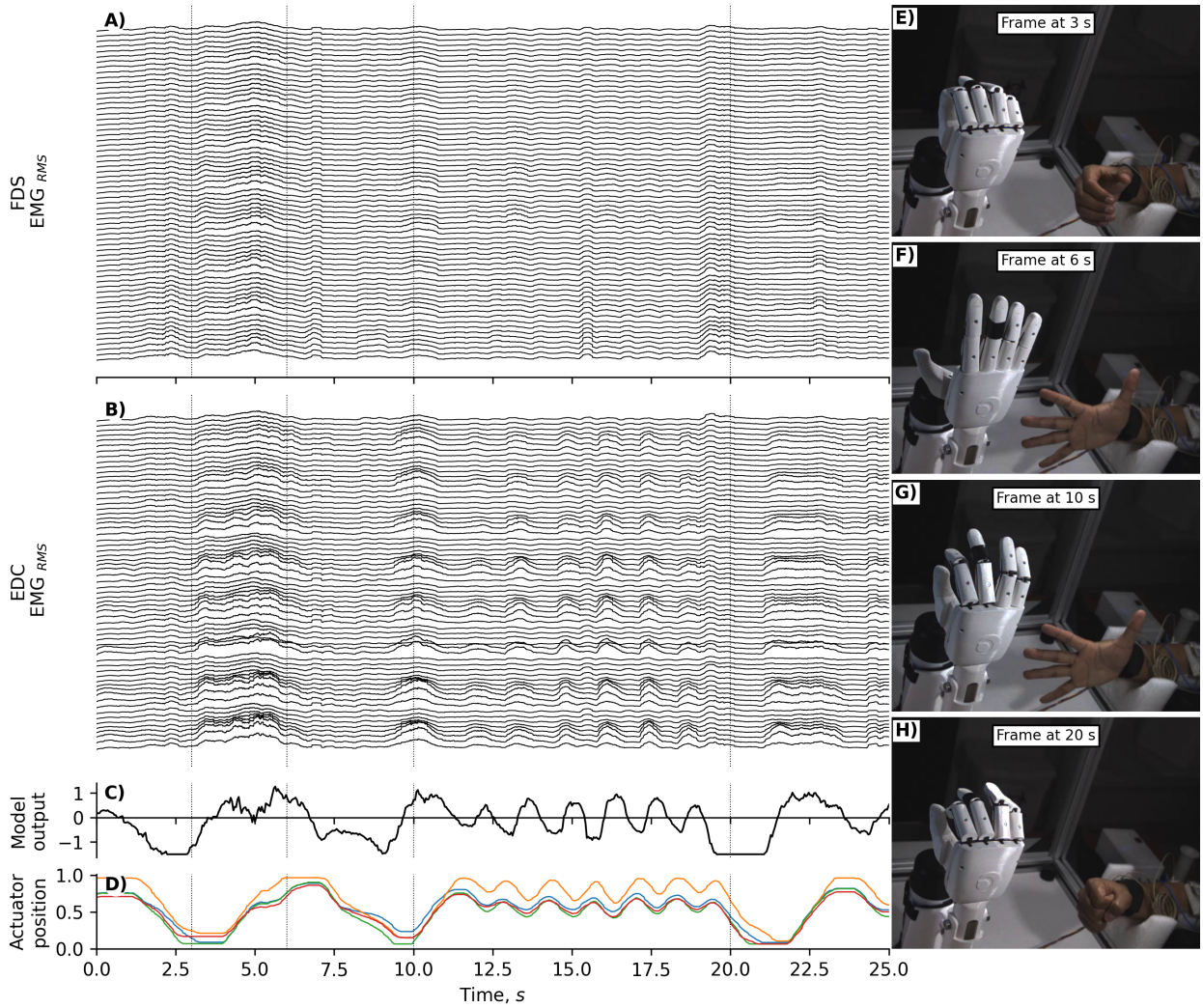

Fig. 7. Illustrative example of real-time myoelectric control of the bionic hand during a 5-finger grasp task. (A) $\boldsymbol{sEMG_{RMS}}$ recorded from the electrode grid positioned over the *Flexor Digitorum Superficialis* (FDS) muscle. (B) $\boldsymbol{sEMG_{RMS}}$ from the electrode grid over the *Extensor Digitorum Communis* (EDC) muscle. (C) Output of the Proportional Movement Intention Decoding (PMID) loop. (D) Position of the bionic hand actuator shafts corresponding to the thumb (blue), index (orange), middle (green), and ring-pinky fingers (red); (E) to H) Video frames synchronized with the HD sEMG recordings, showing the bionic hand and the participant operating the myoelectric control system at 3 s, 6 s, 10 s, and 20 s, respectively (also indicated by vertical lines in the plots).

C. Proportional Movement Intention Decoding Loop

The PMID loop demonstrated that the system successfully reconstructed the dynamics of the modulating signals, achieving high values of R^2 and XC_{max}, particularly in tasks involving grasping movements. Still, these findings would not necessarily imply higher performance in motor tasks representing daily activities [4]. The higher R^2 values observed in grasping tasks likely result from their reduced synergistic control, which facilitates the separability of 1-DoF patterns during the NMF stage. In contrast, non-grasping movements often require additional muscular contractions to stabilize the fingers that are not actively engaged in the task. These postural contractions distribute control more broadly and induce multi-modal motor unit activity shaped by hand configuration. Such complexity increases the dimensionality of HD sEMG signals. Unlike the low-dimensional synergistic control characteristic of grasping, it may account for the lower R^2 values observed when modeling 1-DoF movements [29], [30].

The discrepancy between the high explained variance (R^2) in the reconstruction of $sEMG_{RMS}$ signals and the strong similarity (XC_{max} for the test data) between the model output and the command signal observed in the middle finger task reflects an intrinsic limitation of this measure. Surface EMG amplitude metrics such as $sEMG_{RMS}$ are more directly related to the amplitude of motor unit action potentials than to the underlying motor unit activity, thus providing only a coarse approximation of the neural drive to muscle activation [31].

For the tasks analyzed, which involved cyclostationary signals, the cross-correlation function can exhibit multiple peaks separated by integer multiples of the signal period. Consequently, XC_{max} values occurring at lags exceeding the command signal period may result from the signal's inherent periodicity or from intrinsic noise, rather than representing a true physiological delay. This interpretation aligns with theoretical foundations outlined in the literature, which high-

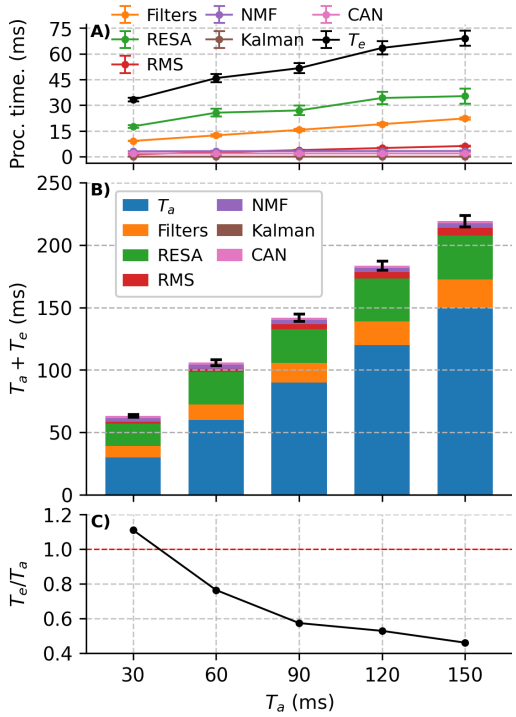

Fig. 8. Processing performance of the Proportional Movement Intention Decoding (PMID) loop as a function of acquisition window ($\boldsymbol{T_a}$). (A) Processing time of each stage, with estimation time ($\boldsymbol{T_e}$) shown in black. (B) Total acquisition and estimation time ($\boldsymbol{T_a + T_e}$), with stacked bars representing the contribution of each processing stage. (C) Ratio of $\boldsymbol{T_e}$ to $\boldsymbol{T_a}$; the red dashed line indicates $\boldsymbol{T_e = T_a}$, with values below the line representing estimation times faster than acquisition. Error bars denote standard deviation. Sample size slightly decreased with $\boldsymbol{T_a}$: $\boldsymbol{N = 66{,}640}$ (30 ms), $\boldsymbol{66{,}560}$ (60 ms), $\boldsymbol{66{,}480}$ (90 ms), $\boldsymbol{66{,}400}$ (120 ms), and $\boldsymbol{66{,}320}$ (150 ms).

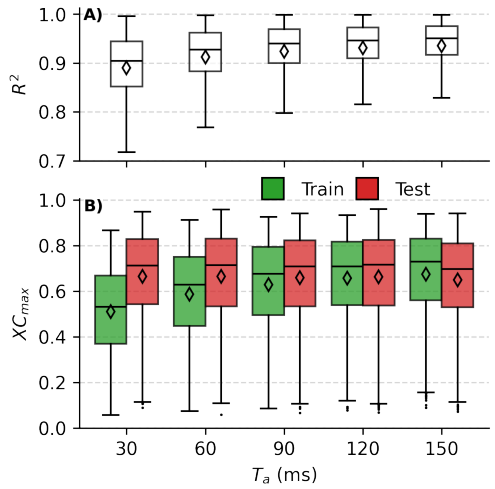

Fig. 9. Performance metrics of the Proportional Movement Intention Decoding (PMID) loop as a function of acquisition windows ($\boldsymbol{T_a}$, $\boldsymbol{N = 1{,}008}$). (A) Distributions of the coefficient of determination ($\boldsymbol{R^2}$) for reconstructing HD sEMG signals from the NMF components. (B) Distributions of the maximum cross-correlation values ($\boldsymbol{XC_{max}}$) between the estimated signals and the command signals for training (green) and testing (red) data. Diamonds denote mean values, boxes represent the interquartile range, and whiskers indicate minimum and maximum values (excluding outliers).

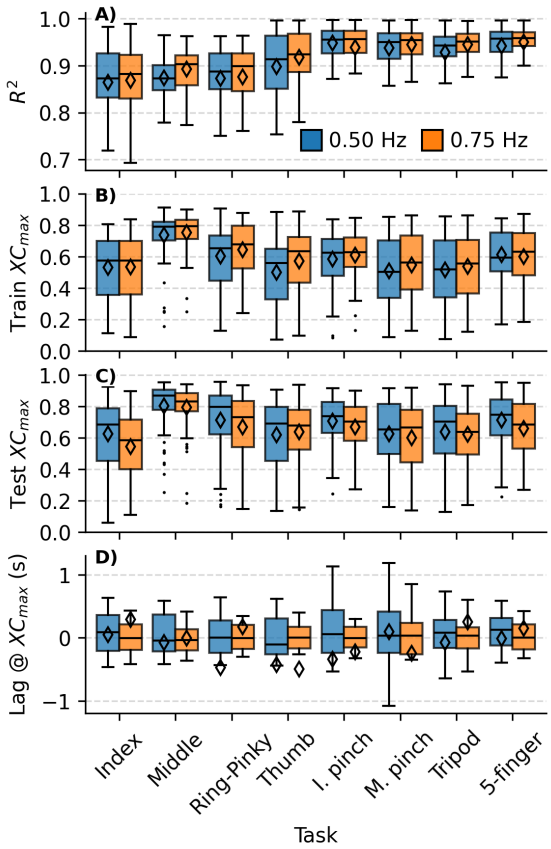

Fig. 10. Distribution of performance metrics for the Proportional Movement Intention Decoding (PMID) loop across different motor tasks and execution frequencies, for $\boldsymbol{T_a = 60}$ ms ($\boldsymbol{N = 63}$). (A) Coefficient of determination ($\boldsymbol{R^2}$) for the reconstruction of HD sEMG signals from NMF components. (B) Maximum cross-correlation value ($\boldsymbol{XC_{max}}$) for the training data. (C) $\boldsymbol{XC_{max}}$ for the test data. (D) Temporal lag at which $\boldsymbol{XC_{max}}$ occurs for the test data. Diamonds represent the mean values, boxes indicate the interquartile range, and whiskers show the minimum and maximum values (excluding outliers).

light the phase ambiguity inherent in periodic signals and the resulting limitations in accurately estimating time delays [32], [33].

VI. ACKNOWLEDGMENTS

The authors would like to thank Mr. Flavio Renato Santos, Mr. Nelio Hilton Gava, and Mr. Glaudson Frade Assunção from the Main Design Lab, Center for Biomedical Engineering, UNICAMP, for their technical support in designing and fabricating the platform and bionic hand prototypes.

REFERENCES

[1] N. Jiang, C. Chen, J. He, J. Meng, L. Pan, S. Su, and X. Zhu, "Bio-robotics research for non-invasive myoelectric neural-interfaces for prosthetic control—a ten-year perspective review," *National Science Review*, 4 2023.

[2] F. Cordella, A. L. Ciancio, R. Sacchetti, A. Davalli, A. G. Cutti, E. Guglielmelli, and L. Zollo, "Literature review on needs of upper limb prosthesis users," *Frontiers in Neuroscience*, vol. 10, no. MAY, pp. 1–14, 2016.

[3] S. Salminger, H. Stino, L. H. Pichler, C. Gstoettner, A. Sturma, J. A. Mayer, M. Szivak, and O. C. Aszmann, "Current rates of prosthetic usage in upper-limb amputees–have innovations had an impact on device acceptance?," *Disability and Rehabilitation*, vol. 44, no. 14, pp. 3708–3713, 2022.

[4] I. Vujaklija, A. D. Roche, T. Hasenoehrl, A. Sturma, S. Amsuess, D. Farina, and O. C. Aszmann, "Translating research on myoelectric control into clinics-are the performance assessment methods adequate?," *Frontiers in Neurorobotics*, vol. 11, no. FEB, pp. 1–7, 2017.

[5] R. C. Sîmpetru, D. I. Braun, A. U. Simon, M. März, V. Cnejevici, D. S. de Oliveira, N. Weber, J. Walter, J. Franke, D. Höglinger, C. Prahm, M. Ponfick, and A. Del Vecchio, "MyoGestic: EMG interfacing framework for decoding multiple spared motor dimensions in individuals with neural lesions," *Science Advances*, vol. 11, no. 15, pp. 1–14, 2025.

[6] E. Rodriguez-Villegas, S. Iranmanesh, and S. A. Imtiaz, "Wearable Medical Devices: High-Level System Design Considerations and Tradeoffs," *IEEE Solid-State Circuits Magazine*, vol. 10, no. 4, pp. 43–52, 2018.

[7] C. Beach, E. Balaban, and A. J. Casson, *Edge algorithms for wearables: An overview of a truly multi-disciplinary problem*. Elsevier Inc., 2 ed., 2020.

[8] R. Merletti and G. L. Cerone, "Tutorial. surface emg detection, conditioning and pre-processing: Best practices," *Journal of Electromyography and Kinesiology*, vol. 54, 10 2020.

[9] E. A. Clancy, E. L. Morin, G. Hajian, and R. Merletti, "Tutorial. Surface electromyogram (sEMG) amplitude estimation: Best practices," *Journal of Electromyography and Kinesiology*, vol. 72, no. June, p. 102807, 2023.

[10] K. Englehart and B. Hudgins, "A Robust, Real-Time Control Scheme for Multifunction Myoelectric Control," *IEEE Transactions on Biomedical Engineering*, vol. 50, no. 7, pp. 848–854, 2003.

[11] M. Stachaczyk, S. F. Atashzar, and D. Farina, "Adaptive spatial filtering of high-density emg for reducing the influence of noise and artefacts in myoelectric control," *IEEE Transactions on Neural Systems and Rehabilitation Engineering*, vol. 28, pp. 1511–1517, 7 2020.

[12] S. Muceli, N. Jiang, and D. Farina, "Extracting signals robust to electrode number and shift for online simultaneous and proportional myoelectric control by factorization algorithms," *IEEE Transactions on Neural Systems and Rehabilitation Engineering*, vol. 22, pp. 623–633, 2014.

[13] R. E. Kalman, "A new approach to linear filtering and prediction problems," *Journal of Fluids Engineering, Transactions of the ASME*, vol. 82, no. 1, pp. 35–45, 1960.

[14] P. Zipp, "Recommendations for the Standardization of Lead Positions in Surface Electromyography*," *European Journal of Applied Physiology and Occupational Physiology*, vol. 50, pp. 41–54, 1982.

[15] E. Farago, D. MacIsaac, M. Suk, and A. D. Chan, "A review of techniques for surface electromyography signal quality analysis," 2023.

[16] C. Sinderby, L. Lindstrom, and A. E. Grassino, "Automatic assessment of electromyogram quality," *Journal of Applied Physiology*, vol. 79, no. 5, pp. 1803–1815, 1995.

[17] J. Chang, A. Phinyomark, and E. Scheme, "Assessment of EMG Benchmark Data for Gesture Recognition Using the NinaPro Database," *Proceedings of the Annual International Conference of the IEEE Engineering in Medicine and Biology Society, EMBS*, vol. 2020-July, pp. 3339–3342, 2020.

[18] M. Tomczak and E. Tomczak, "The need to report effect size estimates revisited. An overview of some recommended measures of effect size," *Trends in Sport Sciences*, vol. 1, no. 21, pp. 19–25, 2014.

[19] S. Mangiafico, *Summary and Analysis of Extension Program Evaluation in R*. Rutgers Cooperative Extension, New Brunswick, NJ, version 1 ed., 2016. Retrieved from `https://rcompanion.org/handbook/`.

[20] T. W. Beck, T. J. Housh, J. T. Cramer, M. H. Malek, M. Mielke, R. Hendrix, and J. P. Weir, "A comparison of monopolar and bipolar recording techniques for examining the patterns of responses for electromyographic amplitude and mean power frequency versus isometric torque for the vastus lateralis muscle," *Journal of Neuroscience Methods*, vol. 166, no. 2, pp. 159–167, 2007.

[21] D. A. Gabriel, "Effects of monopolar and bipolar electrode configurations on surface EMG spike analysis," *Medical Engineering and Physics*, vol. 33, pp. 1079–1085, nov 2011.

[22] R. G. Molinari, F. R. Santos, and L. A. Elias, "Quality assessment of high-density surface myoelectric recordings from a new wearable electrophysiological signal acquisition and processing system for human-machine interfaces," in *XXIX Congresso Brasileiro de Engenharia Biomédica*, pp. 728–729, 2024.

[23] G. L. Cerone, A. Botter, and M. Gazzoni, "A modular, smart, and wearable system for high density sEMG detection," *IEEE Transactions on Biomedical Engineering*, vol. 66, no. 22, pp. 3371–3380, 2019.

[24] S. Koutsoftidis, D. Y. Barsakcioglu, K. Petkos, D. Farina, and E. M. Drakakis, "Myolink: A 128-Channel, 18 nV/$\sqrt{Hz}$, Embedded Recording System, Optimized for High-Density Surface Electromyogram Acquisition," *IEEE Transactions on Biomedical Engineering*, vol. 69, pp. 3389–3396, nov 2022.

[25] T. Stuart, J. Hanna, and P. Gutruf, "Wearable devices for continuous monitoring of biosignals: Challenges and opportunities," *APL Bioengineering*, vol. 6, no. 2, pp. 1–15, 2022.

[26] P. Gkonis, A. Giannopoulos, P. Trakadas, X. Masip-Bruin, and F. D'Andria, "A Survey on IoT-Edge-Cloud Continuum Systems: Status, Challenges, Use Cases, and Open Issues," *Future Internet*, vol. 15, no. 12, pp. 1–27, 2023.

[27] H. Bernhard, H. Seyhan, M. Wagner, and Z. Rainer, *Hand and Wrist anatomy and Biomechanics - A Comprehensive Guide*. Thieme, frist edit ed., 2016.

[28] M. Porta, C. Filetti, A. Chiari, I. Leo, E. Padua, G. Briotti, G. Messina, W. Moalla, and B. Ruscello, "Examining the association between speed and myoelectric activity: Time-based differences and muscle group balance," *PLOS ONE*, vol. 19, 2024.

[29] E. J. Weiss and M. Flanders, "Muscular and postural synergies of the human hand," *Journal of Neurophysiology*, vol. 92, no. 1, pp. 523–535, 2004.

[30] S. Tanzarella, S. Muceli, A. Del Vecchio, A. Casolo, and D. Farina, "Non-invasive analysis of motor neurons controlling the intrinsic and extrinsic muscles of the hand," *Journal of Neural Engineering*, vol. 17, aug 2020.

[31] E. Martinez-Valdes, F. Negro, D. Falla, A. M. De Nunzio, and D. Farina, "Surface electromyographic amplitude does not identify differences in neural drive to synergistic muscles," *Journal of Applied Physiology*, vol. 124, no. 4, pp. 1071–1079, 2018.

[32] W. A. Gardner, "The spectral correlation theory of cyclostationary time-series," *Signal Processing*, vol. 11, no. 1, pp. 13–36, 1986.

[33] E. Efimov, "On the Effect of a Signal Delay on Cross-Spectral Correlation Function," *2022 Systems of Signals Generating and Processing in the Field of on Board Communications, SOSG 2022 - Conference Proceedings*, vol. 2, pp. 1–6, 2022.